PCCP

Accepted Manuscript

ROYAL SOCIETY OF CHEMISTRY

www.rsc.org/pccp

PCCP

RSCPublishing

ARTICLE

Oxygen-doped porous silicon carbide sphere as electrode material for supercapacitors

Cite this: DOI: 10.1039/x0xx00000x

Myeongjin Kim, Hyun Ju and Jooheon Kim*

Received 00th January 2012,
Accepted 00th January 2012

DOI: 10.1039/x0xx00000x

www.rsc.org/

Oxygen-containing functional groups were introduced on the surface of micro- and meso-porous silicon carbide sphere (MMPSiC) in order to investigate the relationship between the electric double layer properties and pseudo-capacitive properties; the degree of oxidation of MMPSiC was also optimized. Although the oxygenated surface functionalities can lead to a decrease in the surface area of MMPSiC, the oxygen functional groups attached to the external surface can participate in the redox reaction, resulting in enhancement of the total super-capacitive performance. The MMPSiC electrode oxidized for 24 h exhibits a high charge storage capacity with a specific capacitance of 301.1 F g^{-1} at a scan rate of 5 mV s^{-1}, with 86.8% rate performance from 5 to 500 mV s^{-1} in 1 M KCl aqueous electrolyte. This outstanding capacitive performance of the MMPSiC electrode oxidized for 24 h can be attributed to the harmonious synergistic effect between the electric double layer capacitive contribution of MMPSiC and the pseudo-capacitive contribution of the oxygen-containing functional groups. These encouraging results demonstrate that the MMPSiC electrode oxidized for 24 h is a promising candidate for high performance electrode materials for supercapacitors.

1. Introduction

Electrochemical capacitors, also known as supercapacitors, have drawn intensive research attention as ideal energy storage devices due to their significant advantages, including high power density, long cycle-life, and safety tolerance to high rate charge and discharge.[1-3] Supercapacitors can be classified into two types according to the energy storage mechanism, namely electric double-layer capacitors (EDLCs) and pseudocapacitors. The capacitance of the former arises from an electrical double layer at the interface between the electrode and electrolyte, whereas that of the latter is due to fast and reversible faradic reactions at the electrode surface.[4] Currently, most commercial supercapacitors are symmetric EDLCs based on high-surface-area carbon materials.[5] However, in most practical applications, EDLCs with porous carbon electrodes suffer from limited energy density, which is typically of the order of 4–5 Wh kg^{-1} for fully assembled cells; this is an order of magnitude lower than that of batteries.[6] Therefore, to solve these problems, scientists have attempted to increase the capacitance by employing materials with high surface area and excellent electrical conductivity.

An effective strategy for obtaining high energy density electrode materials is to control the structure and morphology of porous electrode materials to achieve high surface area and efficient paths for ion diffusion. Moreover, a significant decrease in the internal resistance of the electrode can be achieved by using electrode materials with excellent electrical conductivity due to the formation of a conductive network; this high conductivity can facilitate the application of electrostatic charges, which favors accumulation of the electric double layers.[7] In order to obtain a high surface area, porous carbonaceous materials such as activated carbon, carbide-derived carbons, ordered mesoporous carbons, and carbon aerogels have been studied as high-surface area electrodes for EDLCs. However, the low electrical conductivity of these materials may hinder the formation of a conductive network (which decreases the internal resistance of the electrode) and obstruct the application of electrostatic charges on the surface of the electrode (which form the electric double layer).

Recently, we reported novel three-dimensional silicon carbide-based frameworks with hierarchical micro- and meso-porous structures (MMPSiC) prepared by the template method and carbonization reaction via the aerosol-spray drying technique. The MMPSiC electrode exhibited excellent charge storage capacity with a specific capacitance of 253.7 F g^{-1} at a scan rate of 5 mV s^{-1} with 87.9% rate performance from 5 to 500 mV s^{-1} in 1 M Na_2SO_4 aqueous electrolyte.[8] The excellent electrochemical properties of the MMPSiC electrode are attributed to the following: (i) the mesopores of PSF provide low-resistance pathways for ion diffusion in the pores and good charge propagation, leading to improved capacitive activity. (ii) The abundant micropores play an essential role for optimizing the electrical double layer surfaces and enhancing the capacitance. (iii) The high surface area and pore volume of PSF derived from the dual-pore system (micro/mesoporous) is favorable for furnishing the electrochemically available surface area required for charge accumulation and facilitating the transport of electrolyte ions, thus remarkably improving the electrochemical performance.

(iv) The excellent electrical conductivity of PSF can significantly decrease the internal resistance of an electrode by the construction of a conductive network and facilitate application of electrostatic charges; these features are favorable for accumulating the electric double layers.[9-11] Moreover, the capacitive performance of MMPSiC can be greatly enhanced by the combination of MMPSiC with redox pseudocapacitive materials.[12]

It is well known that synergetic effects may be achieved when the capacitive charging of the double-layer overlaps with a faradic redox (pseudocapacitive) reaction(s) and the two storage mechanisms work in parallel.[13] The introduction of oxygen functional groups into EDLC materials as a pseudocapacitive component is the simplest approach to induce faradic redox reaction.[14] Recent studies have shown that oxygen-functionalized nanocarbons, including carbon nanotubes (CNTs)[15] and reduced graphene oxide[16], can enhance the energy density of carbon electrodes due to surface redox reactions between the oxygen groups and electrolyte ions. However, in the case of porous materials, it is essential to consider the relationship between the electric double layer capacitive contribution and the pseudo-capacitive contribution because the introduced oxygen functionalities cause a decrease in the specific surface area and pore volume by blocking the small micropores.[17] Therefore, although the oxygenated surface functionalities can lead to a decrease in the surface area, the oxygen functional groups attached to the external surface of porous electrode materials can participate in the redox reaction, resulting in an enhancement of the total super-capacitance. However, excessive oxidation of porous materials causes a dramatic decrease of the micropore surface area and pore volume due to the large amount of introduced oxygen functional groups; this is unfavorable for optimizing the electrical double layer surfaces and enhancing the capacitance, resulting in a decline of the total capacitive performance. Therefore, it is essential to optimize the degree of oxidation of the porous materials to maximize the supercapacitance.[18]

Herein, we introduce oxygen-containing functional groups onto the surface of MMPSiC in order to investigate the relationship between the electric double layer capacitive contribution and the pseudo-capacitive contribution and evaluate the optimal degree of oxidation of MMPSiC. The MMPSiC electrode oxidized for 24 h exhibits excellent electrochemical performance derived from the harmonious synergistic effects between the electric double layer properties of MMPSiC and the pseudo-capacitive properties conferred by the oxygen functionalities attached to the MMPSiC surface. We thus achieved a high charge storage capacity with a specific capacitance of 301.1 F g^{-1} at a scan rate of 5 mV s^{-1} with 86.8% rate performance from 5 to 500 mV s^{-1} in 1 M KCl aqueous electrolyte. These encouraging results indicate that the MMPSiC electrode oxidized for 24 h possesses potential advantages for application as an EDLC electrode material with high energy and power density.

2. Experimental

2.1 Synthesis of oxidized micro and mesoporous silicon carbide spheres

MMPSiC samples were prepared by the template method and carbonization reaction via the aerosol-spray drying technique as described in our recent publication.[8] In a typical process, 0.917 g of Si nanoparticles (of about 5 nm) was dispersed in 33 mL of deionized (D.I.) water. Subsequently, 0.014 mL of hydrogen chloride (HCl), 43.3 mL of ethanol (C_2H_5OH), and 1.9742 g of $C_{16}H_{33}(EO)_{20}H$ (Brij56) were added and stirred for 1 h. The resulting solution mixture was ultrasonically sprayed with a home humidifier (60 MHz and 35 W). The droplets were carried by argon (Ar) gas (purity: 99.999%) at a flow rate of 100 sccm (standard cubic centimeter per minute) into a tubular reactor. The tubular reactor was separated into two segments, namely the drying zone and heating zone. The drying-zone tubular reactor (30 mm in diameter and 700 mm in length) was heated up to 150 °C; the heating-zone tubular reactor (30 mm in diameter and 1000 mm in length) was heated up to 1250 °C. At the entrance of the heating zone, C_2H_5OH was ultrasonically and carried by Ar gas at a flow rate of 60 sccm. The particles were recovered by filtration at the outlet of the heating-zone tubular reactor. After terminating the reaction and cooling the reactor to room temperature, the resulting products were exposed to air and heated to 600 °C for 4 h to eliminate the superfluous carbon. Finally, the SiO_2 layer adsorbed on the surface of the MMPSiC particles was removed by treatment with hydrofluoric acid (HF). MMPSiC powder (10 g) was placed in 300 mL of 10% HF solution and stirred for 24 h. The sample was then leached with distilled water until the pH of the leaching water reached a value of 7–8. In order to introduce the oxygen-containing functional groups on the MMPSiC surface, HF-treated MMPSiC powder was dispersed in 34% hydrogen peroxide (H_2O_2) solution and heated to 85 °C for 20, 24, 28, or 32 h with vigorous stirring. The resulting mixture was filtered, washed several times, and dried in a vacuum oven at 60 °C for 24 h. The resultant oxidized micro- and meso-porous silicon carbide sphere (OMMPSiC) materials are denoted as OMMPSiC-*H*, where *H* indicates the oxidation time.

2.2 Characterization methods

X-ray diffraction (XRD) patterns were collected using a New D8-Advance/Bruker-AXS diffractometer at a scan rate of 1° s^{-1} within the 2θ range of 10°–80° using $CuK_{\alpha 1}$ radiation (0.154056 nm). X-ray photoelectron spectroscopy (XPS) analysis was performed on a VGMicrotech ESCA2000 system using a spectrometer with a Mg Kα X-ray source (1253.6 eV) and a hemispherical analyzer. During the curve fitting, the Gaussian peak widths were constant in each spectrum. Nitrogen sorption analysis was performed using an ASAP 2020 accelerated surface area and porosimetry instrument (Micromeritics) equipped with an automated surface area analyzer at 77 K; Brunauer–Emmett–Teller (BET) calculations were used for the surface area. The pore-size distribution plots were recorded from the desorption branch of the isotherms based on the nonlocal density functional theory (NLDFT).

2.3 Preparation and characterization of supercapacitors

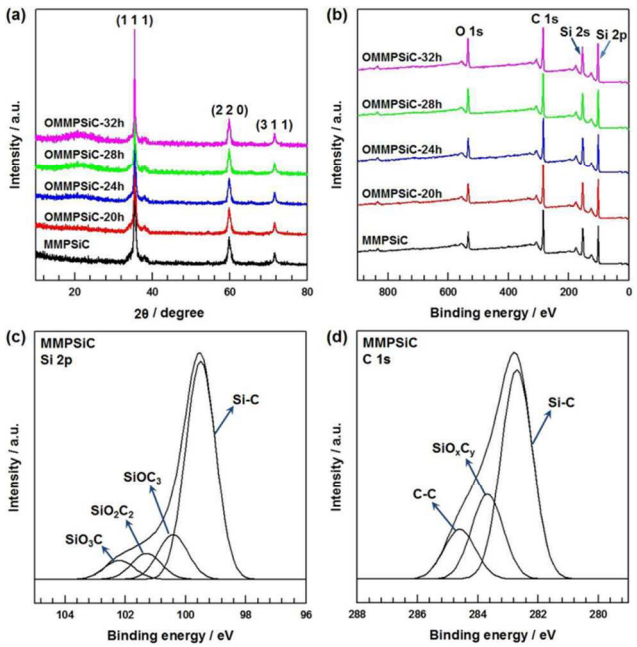

Figure 1. (a) XRD patterns of MMPSiC, OMMPSiC-20h, OMMPSiC-24h, OMMPSiC-28h, and OMMPSiC-32h. (b) XPS wide scan survey spectra of MMPSiC, OMMPSiC-20h, OMMPSiC-24h, OMMPSiC-28h, and OMMPSiC-32h. (c) Deconvoluted XPS Si 2p spectra of MMPSiC. (d) Deconvoluted XPS C 1s spectra of MMPSiC.

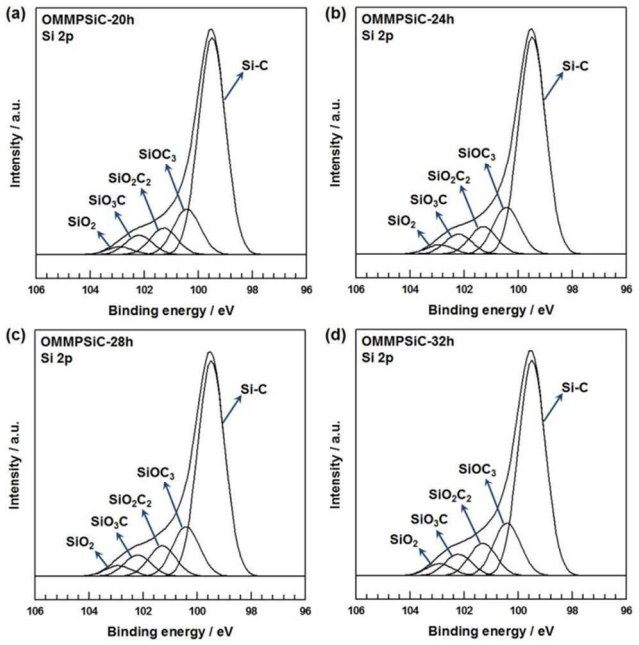

Figure 2. (a) Deconvoluted XPS Si 2p spectra of OMMPSiC-20h. (b) Deconvoluted XPS Si 2p spectra of OMMPSiC-24h. (c) Deconvoluted XPS Si 2p spectra of OMMPSiC-28h. (d) Deconvoluted XPS Si 2p spectra of OMMPSiC-32h.

The working electrodes were fabricated as follows. The resultant powder was mixed with poly(tetrafluoroethylene) (60 wt% aqueous suspension) to form an electrode consisting of 85 wt% active materials, 10 wt% carbon black, and 5 wt% binder. The resulting mixture was then coated onto a stainless steel foil substrate (1 cm × 1 cm) and dried in a vacuum oven at 60°C for 6 h. The loading mass of each electrode was approximately 6 mg. In a three-electrode cell, the stainless steel foil substrate (loaded as described above), a platinum foil, and a Ag/AgCl (KCl-saturated) electrode were used as the working, counter, and reference electrodes, respectively. All measurements, including cyclic voltammetry (CV), galvanostatic charge/discharge characteristics, and electrochemical impedance spectroscopy (EIS) measurements, were performed in 1 M KCl aqueous solution at room temperature using a CHI 660C electrochemical workstation. EIS measurements were carried out by applying an AC voltage with 5 mV amplitude in the frequency range of 0.001 to 10^5 Hz at open-circuit potential.

3. Results and Discussion

The X-ray diffraction (XRD) patterns of MMPSiC, OMMPSiC-20h, OMMPSiC-24h, OMMPSiC-28h, and OMMPSiC-32h are shown in Figure 1(a). The XRD pattern of MMPSiC shows three β-SiC peaks at 2θ = 35.6°, 60°, and 71.7°, which were assigned to the (1 1 1), (2 2 0), and (3 1 1) reflections, respectively, and correlated to the face-centered cubic (fcc) β-SiC structure in accordance with the reference data (JCPDS 29-1129, a = 4.3589 Å).[16] After oxidation of MMPSiC, broad SiO_2 peak emerged around at 2θ = 25° for all the OMMPSiC samples. Moreover, the SiO_2 peaks for OMMPSiC are gradually pronounced with the increase of the oxidation time, as further confirmed by the X-ray photoelectron spectroscopy (XPS) analysis. Figure 1(b) shows the XPS wide scan spectra of MMPSiC, OMMPSiC-20h, OMMPSiC-24h, OMMPSiC-28h, and OMMPSiC-32h. An O-based bond (O 1s peak), C-based bond (C 1s peak), and a Si-based bond (Si 2s and Si 2p peak) were detected in the overall XPS spectra for all samples in the binding energy (E_b) region of 0–900 eV. The O 1s (E_b = near 532 eV), C 1s (E_b = near 285 eV), Si 1s (E_b = near 150 eV), and Si 2p (E_b = near 100 eV) peaks are shown in Figure 1(b). The surface oxygen contents of OMMPSiC increased with increasing oxidation time, as judged from the enhancement of the intensity of the O 1s peak, which became predominant. The high-resolution spectra of these peaks are analyzed in detail below to investigate the difference in the surface structure of the five SiC samples. To obtain the detailed surface information, the Si 2p and C 1s core-level spectra of MMPSiC and OMMPSiC were deconvoluted and the results are shown in Figure 1(c), 1(d), 2, 3 and listed in Table S1 and S2. Moreover, the relative atomic percentage was obtained by taking the ratio of each peak area in the Si 2p and C 1s core-level spectra. The Si 2p region of the spectrum acquired for the surface of MMPSiC showed that apart from the strong Si–C peak at the binding energy of 99.5 eV, some intermediate oxidation products of SiC were also present on the surface. These were assigned as $SiOC_3$ at 100.42 eV, SiO_2C_2 at 101.3 eV, and SiO_3C at 102.2 eV (Figure 1(c)). The C 1s core level of MMPSiC showed strong binding energy peaks of the Si–C bonds at 282.7 eV and C–C bonds at 284.6 eV, with several binding energy peaks of SiO_xC_y at 283.68 eV (Figure 1(d)). However, as shown in Figure 2, the SiO_2 peak emerged at a binding energy of 102.92 eV and the areas of the

SiO_2 peaks as well as the silicon oxycarbide (SiC_xO_y) peaks gradually increased with increasing oxidation time.[19] Furthermore, as shown in Figure 3, a new peak corresponding to the C-OH/C-O-C groups emerged at 285.73 eV, indicating that the oxygen-containing functional groups were effectively introduced onto the OMMPSiC surface. Moreover, the area of the SiC_xO_y peak in the C 1s spectrum also increased slightly, which is in good agreement with the behavior of the $SiOC_3$, SiO_2C_2, and SiO_3C peaks in the Si 2p spectra. Importantly, with increasing oxidation time, the area of the peak associated with C-OH/C-O-C in the C 1s spectra became predominant, indicating that a larger number of oxygen groups was introduced in proportion with the oxidation time.

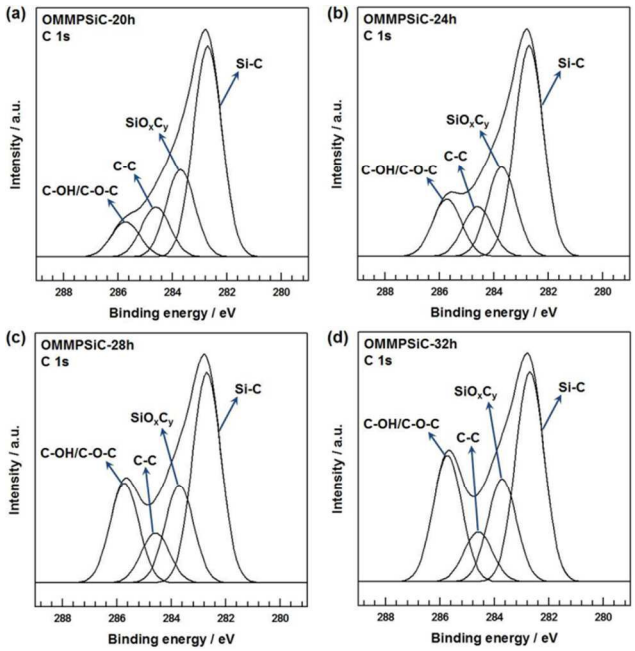

Figure 3. (a) Deconvoluted XPS C 1s spectra of OMMPSiC-20h. (b) Deconvoluted XPS C 1s spectra of OMMPSiC-24h. (c) Deconvoluted XPS C 1s spectra of OMMPSiC-28h. (d) Deconvoluted XPS C 1s spectra of OMMPSiC-32h.

The porous nature of the electrode material is the crucial factor that determines the electrochemical performance of a supercapacitor. Brunauer-Emmett-Teller (BET) and nonlocal density functional theory (NLDFT) analyses were employed to investigate the surface area and pore structure of MMPSiC and OMMPSiC. As shown in Figure S1 ~ S5, the isotherms for all samples show a sharp increase at low P/P_0, demonstrating the existence of micropores. A hysteresis loop was observed at partial pressures above P/P_o = 0.4 with an adsorption plateau near P/P_o = 1.0, indicating the presence of mesopores.[20] Moreover, the pore-size distribution indicates that the nanopores for all samples can be divided into micro- and meso-pore regions, which is in good agreement with the N_2 isotherms. With increasing oxidation time, the amount of N_2 adsorbed by OMMPSiC based on the N_2 adsorption/desorption isotherm and the integrated area of the differential pore volume for OMMPSiC in the pore size distribution decreased, indicating that the specific surface area and pore volume decreased in proportion with the oxidation time. Interestingly, the pore size distribution of all OMMPSiC samples indicates an obvious decrease in the pore volumes in the micropore region, whereas the pore volumes in the mesopore region decreased slightly because the micropores are easily blocked by the introduced oxygen functional groups due to the small pore size. Figure 4 shows the dependence of the specific surface area and pore volume on the oxidation time. The porosity of the resultant OMMPSiC was significantly influenced by the introduced oxygen-containing functional groups depending on the oxidation time. The specific surface area and pore volume of OMMPSiC decreased with increasing oxidation time, indicating that the introduction of oxygen-containing functional groups into the micropores hindered the access of N_2 into some of these pores. For oxidation times of up to 24 h, the surface area and pore volume decreased slightly, whereas beyond 24 h, the surface area and pore volume decreased dramatically due to the introduction of a large amount of oxygen functional groups. As shown in Figure 3 (C 1s spectra), the peak areas associated with C-OH/C-O-C increased gradually with increasing oxidation time up to 24 h. However, beyond 24 h, the intensity of the peak corresponding to the oxygen functional group component of OMMPSiC increased dramatically, indicating the introduction of a large number of oxygen functional groups. This large amount of oxygen functionalities blocked the micropores, resulting in a dramatic decrease of the specific surface area and pore volume. Therefore, it can be expected that the differences in the micro- and meso-pore surface area and pore volume depending on the oxidation time of MMPSiC should lead to significant differences in the ion diffusion/transport phenomenon during the charging/discharging process, resulting in different electrochemical properties.[21]

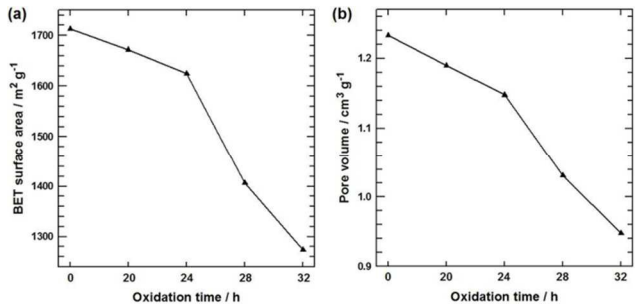

Figure 4. (a) BET surface area behavior as a function of OMMPSiC oxidation time. (b) Pore volume behavior as a function of OMMPSiC oxidation time.

The electrochemical performance of MMPSiC and OMMPSiC as supercapacitor electrodes was characterized by cyclic voltammetry (CV), galvanostatic charge/discharge measurement, and electrochemical impedance spectroscopy (EIS). Figure 5(a) shows the CV curves of the MMPSiC, OMMPSiC-20h, OMMPSiC-24h, OMMPSiC-28h, and OMMPSiC-32h electrodes, acquired at a scan rate of 5 mV s^{-1} with potential windows ranging from 0 to 1 V (vs. Ag/AgCl) in 1 M KCl aqueous solution. The CV curve for the MMPSiC electrode shows a nearly rectangular shape without obvious redox peaks, indicative of ideal electric double layer capacitive behavior due to the harmonious electrochemical environment derived from the dual pore system (micro- and meso-pores). The abundant micropores in MMPSiC play an essential role in optimizing the electrical double layer surfaces and enhancing the

capacitance, whereas the mesopores of MMPSiC provide low-resistance pathways for ion diffusion in the pores and good charge propagation, leading to improved capacitive activity. Based on comparison of the shape of the CV curve, the MMPSiC electrode give rise to an ideally rectangular shape, whereas all the OMMPSiC electrodes show cathodic and anodic humps during the charge/discharge process, indicating that the redox reactions may occur via oxygenated surface functionalities, such as the quinone/hydroquinone (Q/HQ) pair or pyrone-like structures.[21] Figure 5(b) shows the galvanostatic charge/discharge curves for the MMPSiC, OMMPSiC-20h, OMMPSiC-24h, OMMPSiC-28h, and OMMPSiC-32h electrodes, acquired at a current density of 0.5 A g^{-1} with potential windows ranging from 0 to 1 V. The charge-discharge curve of the MMPSiC electrode shows a good linear relationship between the charge-discharge potentials and time, indicating a rapid I-V response and ideal capacitive characteristics. However, the charge curves for the OMMPSiC electrodes show slight curvature in the low potential region and are almost symmetrical to their corresponding discharge counterparts, indicating pseudocapacitive and electric double layer capacitive contribution, which shows good agreement with the CV curve behavior.

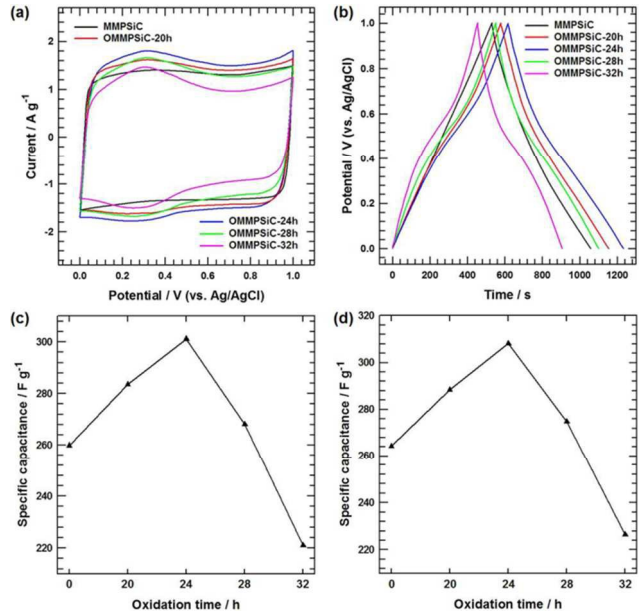

Figure 5. (a) CV curves for MMPSiC, OMMPSiC-20h, OMMPSiC-24h, OMMPSiC-28h, and OMMPSiC-32h electrodes at a scan rate of 5 mV s^{-1}. (b) Galvanostatic charge/discharge curves for MMPSiC, OMMPSiC-20h, OMMPSiC-24h, OMMPSiC-28h, and OMMPSiC-32h electrodes at a current density of 0.5 A g^{-1}. (c) specific capacitance as a function of the OMMPSiC oxidation time, obtained from the CV curve at a scan rate of 5 mV s^{-1}. (d) specific capacitance as a function of the OMMPSiC oxidation time, obtained from the galvanostatic charge/discharge curves at a current density of 0.5 A g^{-1}.

The specific capacitances (C_s) are calculated from the CV and galvanostatic charge-discharge curves using equation (1) and (2):[25,26]

$$C_s = \frac{1}{v(V_c - V_a)} \int_{V_a}^{V_c} I(V)dV \quad (1)$$

$$C_s = \frac{\mathrm{I} \times \mathrm{t}}{\mathrm{m} \times \Delta \mathrm{V}} \quad (2)$$

where C_s is the specific capacitance (F g^{-1}), v is the potential scan rate (mV s^{-1}), $V_c - V_a$ represents the sweep potential range (V), I(V) denotes the response current density (A g^{-1}), I is the discharge current, t is the discharge time, m is the mass of active material, and ΔV is the voltage drop upon discharging. Figure 5(c) and (d) show the specific capacitance as a function of the oxidation time, obtained from the CV curve acquired at a scan rate of 5 mV s^{-1} and the galvanostatic charge-discharge curves acquired at a current density of 0.5 A g^{-1}, respectively. In both Figure 5(c) and (d), for oxidation times of up to 24 h, the C_s values for the OMMPSiC electrodes gradually increased, whereas beyond 24 h, the C_s values decreased dramatically. These observations indicate that the OMMPSiC-24h electrode exhibits the highest specific capacitance performance because of the synergistic effect between the electrical double layer capacitive contribution by MMPSiC and the pseudo-capacitive contribution derived from the introduced oxygen-containing functional groups on the MMPSiC surface. Although the surface area and pore volume decreased slightly with extended oxidation time, the C-OH/C-O-C groups that were mainly attached to the external surface play an important role in the charging/discharging process, as they provide a passage for the ions to reach the internal surface of the electrodes.[22] These functional groups were also reported to be responsible for fast redox reactions at or near the electrode surface, which gives rise to the pseudocapacitance. In addition, the interactions between the electrolyte and the MMPSiC surface increased because the SiO_2 layer improves the hydrophilicity of MMPSiC. This in turn provides MMPSiC with better accessibility to the electrolyte ions, resulting in the fast reaction kinetics.[23] However, when MMPSiC was oxidized for more than 24 h, the specific capacitance of the OMMPSiC-28h and OMMPSiC-32h electrodes decreased dramatically due to the dramatically decreased electric double layer contribution. The cathodic and anodic humps in Figure 5(a) were more pronounced in the case of the OMMPSiC-28h and OMMPSiC-32h electrodes, indicating vigorous redox-reactions induced by the oxygen functional groups due to the high population of oxygen functional groups. However, the dramatically decreased micropore surface area and pore volume derived from the large amount of introduced oxygen functional groups is not advantageous for optimizing the electrical double layer surfaces and enhancing the capacitance, resulting in a decrease in the total capacitive performance.[24] Therefore, the excellent electrochemical performance of the OMMPSiC-24h electrode could be ascribed to the following characteristics: (i) because of its large surface area, OMMPSiC-24h provides sufficient electrode/electrolyte interfaces for charge accommodation. (ii) The presence of oxygen-containing functional groups on the OMMPSiC-24h surface may yield stable pseudo-capacitance through faradic charge-transfer reactions. (iii) The presence of the oxygen and SiO_2 layer enhances the surface wettability of OMMPSiC-24h to ensure adequate utilization of the exposed surface for charge storage.

To further investigate the rapid charge/discharge characteristics, the OMMPSiC-24h electrode was subjected to detailed measurements. Figure 6(a) and (b) present the CV curves and

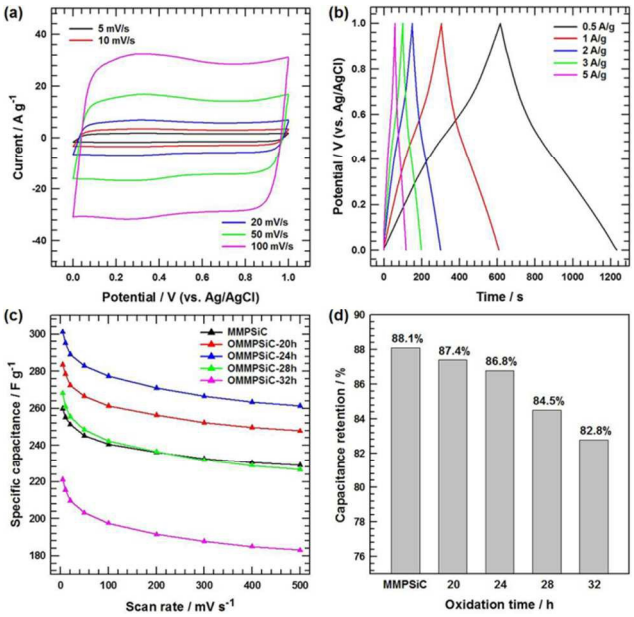

Figure 6. (a) CV curves of OMMPSiC-24h electrode at different scan rates. (b) Galvanostatic charge/discharge curves of OMMPSiC-24h electrode at different current densities. (c) Specific capacitances for MMPSiC, OMMPSiC-20h, OMMPSiC-24h, OMMPSiC-28h, and OMMPSiC-32h electrodes at different scan rates. (d) The capacitance retention ratio as a function of the potential scan rates from 5 to 500 mV s^{-1} for MMPSiC, OMMPSiC-20h, OMMPSiC-24h, OMMPSiC-28h, and OMMPSiC-32h electrodes.

galvanostatic charge-discharge curves of the OMMPSiC-24h electrode acquired at various scan rates and current densities, respectively. The cathodic and anodic humps presented in Figure 6(a) became weaker when the CV curves were acquired at high scan rates. Moreover, the slight curvature regions at low potential in the charge/discharge curves acquired at high current densities of the galvanostatic charge/discharge curves were also weakened because access of the ions to the active surface is reduced at high scan rates or current densities, especially for relatively slow faradaic reactions. Figure 6(c) shows the relationship between C_s and the scan rates of the MMPSiC, OMMPSiC-20h, OMMPSiC-24h, OMMPSiC-28h, and OMMPSiC-32h electrodes. It can be clearly seen that the C_s values for all the electrodes decreased steadily with increasing scan rate. With an increase of the scan rate from 5 to 500 mV s^{-1}, rate performance values of 88.1, 87.4, 86.8, 84.5 and 82.8% were respectively obtained for the MMPSiC, OMMPSiC-20h, OMMPSiC-24h, OMMPSiC-28h, and OMMPSiC-32h electrodes, indicating that the capacitance retention of the OMMPSiC electrodes decreased steadily with increasing oxidation time (Figure 6(d)). Apart from the influence from the redox mechanisms induced by the oxygen-containing functional groups, the decrease in the capacitance retention of the highly oxidized OMMPSiC electrodes may also result from the aggregation of ionic species or water molecules to hinder migration of the electrolyte in the micropores.[25] In the presence of a large population of oxygen functionalities, the local electronic charge density of these electrodes could be enhanced by increasing the potential, thus leading to the formation of aggregates.[25] Therefore, these aggregates can result in high-resistance pathways for ion diffusion in the pores, resulting in slow ion transport through the porous network, especially when a large loading current density or scan rate is employed.[10] In general, the nanopore structure of the ideal porous EDLC electrode should have a short ion diffusion distance, providing fast ion transport pathways. In this case, the electrical double layer can be reorganized rapidly at the switching potentials, after which the response current reaches a steady state.[11] However, the CV profiles of the highly oxidized MMPSiC electrodes (OMMPSiC-28h and OMMPSiC-32h) (Figure 5(a)) show an obvious current delay to reach a horizontal value after reversal of the potential sweep, indicating unfavorable ion transfer/diffusion within the porous structure due to the large populations of oxygen-containing functional groups.

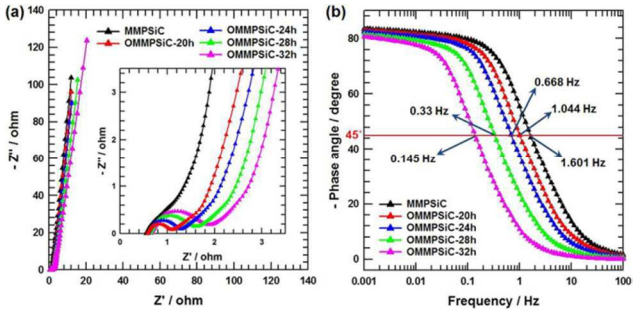

Figure 7. (a) Nyquist plots for MMPSiC, OMMPSiC-20h, OMMPSiC-24h, OMMPSiC-28h, and OMMPSiC-32h electrodes. Inset magnifies the data in the high-frequency range. (b) Impedance phase angle versus frequency for MMPSiC, OMMPSiC-20h, OMMPSiC-24h, OMMPSiC-28h, and OMMPSiC-32h electrodes.

EIS measurements were performed for the MMPSiC, OMMPSiC-20h, OMMPSiC-24h, OMMPSiC-28h, and OMMPSiC-32h electrodes, and the results are presented in Figure 7. The EIS data were analyzed using Nyquist plots (Figure 7(a)). The Nyquist plots show the frequency response of the electrode/electrolyte system and are a plot of the imaginary component (Z") of the impedance against the real component (Z'). The Nyquist plots consist of three parts: (i) a semicircle in the high-to-medium frequency region, with the starting cross-point at the Z′ axis indicating the combined series resistance of the electrolyte, electrode, current collectors, electrode/current collector contact resistance, and the diameter of the semicircle representing the charge transport resistance (R_{ct}).[27] (ii) A straight line with a slope of 45° in the low-frequency range, which corresponds to the semi-infinite Warburg impedance, resulting from the frequency dependence of ion diffusion/transport in the electrolyte.[28] (iii) A vertical line at very low frequencies caused by the accumulation of ions at the bottom of the pores of the electrode.[29] The nearly vertical line indicates good capacitive behavior without diffusion limitations. The Nyquist plot of the MMPSiC electrode is almost vertical at low frequencies with no semicircle in the high frequency region, indicating ideal capacitive performance. However, semicircles emerged in the high frequency region for all OMMPSiC electrodes, indicative of reduced electrical conductivity and faradic reaction because of the introduced oxygen functionalities. Comparison of the OMMPSiC electrodes shows a

major difference in the charge transfer resistance in the high-frequency range and the Warburg and vertical line region in the low-frequency range. In the magnified high- to medium-frequency regions of the Nyquist plots (inset in Figure 7(a)), the charge transport resistance and the Warburg impedance both gradually increase with increasing oxygen content. In addition, as observed in Figure 7(b), the phase angle in the lower-frequency-limitation region for MMPSiC, OMMPSiC-20h, OMMPSiC-24h, OMMPSiC-28h, and OMMPSiC-32h electrodes is -83.5˚, -82.9˚, -82.3˚, -81.4˚ and -80.7˚, showing gradual decrease with increasing the oxidation time, indicating the slow ion diffusion in the electrolyte and ion adsorption on the electrode surface; this result also reveals the presence of high-resistant pathways for the ion diffusion in the pores, as the introduced oxygen functional groups on the MMPSiC surface cause the decrease of the specific surface area and hinder the migration of electrolyte in the micropores. Therefore, these EIS tendencies of the OMMPSiC electrodes are in good agreement with the rate performance behavior presented in Figure 6(d).

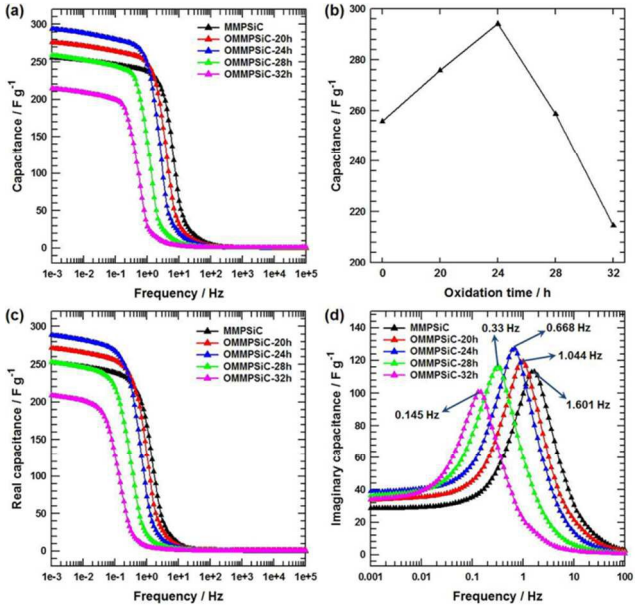

Figure 8. (a) Capacitance as a function of frequency obtained from EIS for MMPSiC, OMMPSiC-20h, OMMPSiC-24h, OMMPSiC-28h, and OMMPSiC-32h electrodes. (b) Capacitance as a function of the OMMPSiC oxidation time, obtained from EIS at a frequency of 0.001 Hz. (c) Real part of capacitance as a function of frequency for MMPSiC, OMMPSiC-20h, OMMPSiC-24h, OMMPSiC-28h, and OMMPSiC-32h electrodes. (d) Imaginary part of capacitance as a function of frequency for MMPSiC, OMMPSiC-20h, OMMPSiC-24h, OMMPSiC-28h, and OMMPSiC-32h electrodes.

Complex capacitance analysis, which can be easily performed using the impedance spectra, has emerged as an excellent technique for investigating the bulk and interfacial electrochemical properties. Figure 8(a) presents the capacitance–frequency dependence derived from the Nyquist plot according to the following equation:[30]

$$C(f) = \frac{-1}{2\pi f Z''(f)} \quad (3)$$

where f is the frequency, and $Z''(f)$ is the imaginary part of the impedance. The relationship between the capacitance and frequency reflects the penetration of the alternating current into the bulk pores of the electrode material, from which the number of electrolyte ions reaching the pore surfaces at a specific frequency can be evaluated. The MMPSiC and OMMPSiC electrodes reached full capacitance at low frequency, and the capacitance started to decline with increasing frequency. At low frequency, the electrolyte ions can access more of the electrode surface due to deep penetration inside the pores of the electrodes, leading to vigorous faradaic reactions and thereby contributing to the high capacitance value. At higher frequencies, the electrolyte ions could only access the surface of the electrodes, whereas the deeper pores were not accessed, leading to inadequate faradaic reactions and a consequent sharp decrease in the capacitance.[31] The $C(f)$ values of the MMPSiC, OMMPSiC-20h, OMMPSiC-24h, OMMPSiC-28h, and OMMPSiC-32h electrodes at 1 mHz were calculated to be 255.8, 275.8, 294.1, 258.7, and 214.6 F g^{-1}, respectively, where the capacitive performance follows the same order obtained from the CV and galvanostatic charge/discharge tests (Figure 8(b)). In addition, as the frequency increased, the $C(f)$ value of the OMMPSiC-32h electrode declined sharply at the lowest frequency (0.15 Hz) among the OMMPSiC electrodes, indicating that the unfavorable ionic diffusion to the active electrode surface leads to poor rate capability at high frequencies or high scan rates. Plots of the frequency-dependent real ($C'(f)$) and imaginary ($C''(f)$) components of the capacitance were obtained from the impedance spectra according to the following equations:[32]

$$C'(f) = \frac{-Z''(f)}{2\pi f \left|Z(f)\right|^2} \quad (4)$$

$$C''(f) = \frac{Z'(f)}{2\pi f \left|Z(f)\right|^2} \quad (5)$$

where $Z'(f)$ and $Z''(f)$ are the real and imaginary parts of the impedance, respectively, and $|Z(f)|$ is the absolute value of the impedance. As shown in Figure 8(c), the $C'(f)$ curves for the MMPSiC and OMMPSiC electrodes exhibit similar behavior to that of $C(f)$. The time constant (τ_0), which is a characteristic parameter indicating the rate capability of an electrical system, can be estimated from the peak frequency of $C''(f)$ using the following equation:[33]

$$\tau_0 = \frac{1}{f} \quad (6)$$

where f is the frequency corresponding to the peak frequency of the imaginary capacitance. As observed in Figure 8(d), the maximum capacitances ($C''(f)$) for the MMPSiC, OMMPSiC-20h, OMMPSiC-24h, OMMPSiC-28h, and OMMPSiC-32h electrodes were observed at frequencies of 1.601, 1.044, 0.668, 0.33, and 0.145 Hz, yielding corresponding time constants of 0.624, 0.957, 1.497, 3.023, and 6.874 s, respectively. In addition, the peak frequencies of the $C''(f)$ curves for the MMPSiC and OMMPSiC electrodes coincide perfectly with the frequencies at the phase angle of -45˚ (Figure 7(b)). The longest time constant obtained for the OMMPSiC-32h electrode is derived from the unfavorable accessibility of the outer surface of the electrode material to the electrolyte ions, resulting in

poor rate performance.[34] Therefore, the observed trend for the time constants of the OMMPSiC electrodes agrees well with the capacitance retention performance obtained from the CV measurements (Figure 6(c) and (d)).

4. Conclusion

In summary, MMPSiC spheres were synthesized by employing the template method and carbonization reaction using the aerosol spray-drying method. Oxygen-containing functional groups were successfully introduced onto the MMPSiC surface by hydrogen peroxide treatment. The specific surface area, pore volume, and the electrochemical properties of oxygen-functionalized MMPSiC were investigated as a function of the introduced oxygen functional group content. Although the MMPSiC electrode exhibited outstanding rate performance because of the ideal porous structure that can provide a short ion diffusion distance and thus fast ion transport pathways, the OMMPSiC-24h electrode exhibited the highest charge storage capacity. The specific capacitance of the OMMPSiC-24h electrode was 301.1 F g^{-1} at a scan rate of 5 mV s^{-1} with 86.8% rate performance from 5 to 500 mV s^{-1} in 1 M KCl aqueous electrolyte. The outstanding capacitive performance of the OMMPSiC-24h electrode can be attributed to the harmonious synergistic effect between the electric double layer contribution of MMPSiC and the pseudo-capacitive contribution of the oxygen-containing functional groups.

Notes and references

School of Chemical Engineering & Materials Science, Chung-Ang University, 84 Heukseok-Ro, Dongjak-gu, Seoul 156-756, Korea.
E-mail : jooheonkim@cau.ac.kr
Phone : +82-2-820-5763, Fax : +82-2-824-3495

1. V. Subramanian, H. Zhu, R. Vajtai, P. M. Ajayan, and B. Wei, J. Phys. Chem. B, 2005, **109**, 20207-20214.
2. A. C.-G. Karina, L.-C. Monica, C.-P. Nieves, and G.-R. Pedro, *Adv. Funct. Mater.*, 2005, **15**, 1125-1133.
3. A. L. Mohana, R. F. Estaline, A. Imran, and J. S. Ramaprabhu, *Nanoscale Res. Lett.*, 2008, **3**, 145-151.
4. S. Bose, T. Kuila, A. K. Mishra, R. Rajasekar, N. H. Kim, and J. H. Lee, *J. Mater. Chem.*, 2012, **22**, 767-784.
5. H. Jiang, J. Ma, and C. Z. Li, *Adv. Mater.*, 2012, **24**, 4197-4202.
6. A. Burke, *Electrochim. Acta*, 2007, **53**, 1083–1091.
7. L. L. Zhang, R. Zhou, and X. S. Zhao, *J. Mater. Chem.,* 2010, **20**, 5983-5992.
8. M. Kim, I. Oh, and J. Kim, *J. Mater. Chem. A*, 2015, **3**, 3944-3951.
9. Z. S. Wu, Y. Sun, Y.Z. Tan, S. Yang, X. Feng, and K. Mullen, *J. Am. Chem. Soc.,* 2012, **134**, 19532-19535.
10. W. Xiong, M. Liu, L. Gan, Y. Lv, Z. Xu, Z. Hao, and L. Chen, *Colloids Surf. A,* 2012, **411**, 34-39.
11. F. Xu, R. Cai, Q. Zeng, C. Zou, D. Wu, F. Li, X. Lu, Y. Liang, and R. Fu, *J. Mater. Chem.,* 2011, **21**, 1970-1976.
12. W. Xing, S. Z. Qiao, R. G. Ding, F. Li, G. Q. Lu, Z. F. Yan and H. M. Cheng, *Carbon*, 2006, **44**, 216–224.
13. G. Milczarek, A. Ciszewski, and I. Stepniak, *J. Power Sources*, 2011, **196**, 7882-7885.
14. D. Hulicova-Jurcakova, M. Seredych, G.Q. Lu, and T.J. Bandosz, *Adv. Funct. Mater.*, 2009, **19**, 438-447.
15. D. Yu, and L. Dai, *J. Phys. Chem. Lett.*, 2009, **1**, 467-470.
16. Y. Oh, J. Yoo, Y. Kim, J. Yoon, H. Yoon, J. Kim, and S. Park, *Electrochim. Acta*, 2014, **116**, 118-128.
17. A.N.A. El-Hendawy, Car*bon*, 2003, **41**, 713-722.
18. S. Zhu, S. Ding, and R. Wang, *Mater. Lett.*, 2005, **59**, 595-597.
19. G.D. Sorarù, G. D'Andrea, and A. Glisenti, *Mater. Lett.*, 1996 **27**, 1-5.
20. M. Kim, I. Oh, and J. Kim, *Phys. Chem. Chem. Phys.,* 2015, **17**, 4424-4433.
21. G. Milczarek, A. Ciszewski, and I. Stepnaik, *J. Power Sources*, 2011, **196**, 7882-7885.
22. B. Zhao, P. Liu, Y. Jiang, D. Pan, H. Tao, J. Song, T. Fang, and W. Xu, *J. Power Sources*, 2012, **198**, 423-427.
23. J. Chen, J. Zhang, M. Wang, L. Gao, and Y. Li, *J. Alloys Compd.*, 2014, **605**, 168-172.
24. M. Kim, Y. Hwang, K. Min, J. Kim, *Electrochim. Acta*, 2013, **113**, 322-331.
25. X. Xie, and L. Gao, *Carbon,* 2007, **45**, 2365-2373.
26. Y.R. Nian, H. Teng, *J. Electroanal. Chem.*, 2003, **540**, 119-127.
27. S. Rodrigues, N. Munichandraiah, and A K. Shukla, *J.Solid State Electrochem.*, 1999, 3, 397-405.
28. bb. J.O. Iroh, and W. Su, *Electrochimica acta*, 2000, **46**, 15-24.
29. J. Gamby, P.L. Taberna, P. Simon, J.F. Fauvarque, and M. Chesneau, *J. Power Sources*, 2001, **101**, 109-116.
30. H. Randriamahazaka, and K. Asaka, *J. Phys. Chem. C*, 2010, **114**, 17982-17988.
31. M. Biswal, A. Banerjee, M. Deo and S. Ogale, *Energy Environ. Sci.*, 2013, **6**, 1249–1259.
32. I. Stepniak and A. Ciszewski, *Electrochim. Acta*, 2011, **56**, 2477–2482.
33. I. Stepniak and A. Ciszewski, *J. Power Sources*, 2010, **195**, 5130–5137.
34. C. Yang, M. Zhou and Q. Xu, *Phys. Chem. Chem. Phys*., 2013, **15**, 19730–19740.

